Assessing Nontrivial Topology in Weyl Semimetals by Dichroic Photoemission

J. Schusser[1,*] H. Bentmann,[1] M. Ünzelmann,[1] T. Figgemeier,[1] C.-H. Min,[2,3] S. Moser,[4]
J. N. Neu,[5,6] T. Siegrist,[5,7] and F. Reinert[1]

[1]*Experimentelle Physik VII and Würzburg-Dresden Cluster of Excellence ct.qmat, Universität Würzburg, D-97074 Würzburg, Germany*
[2]*Institut für Experimentelle und Angewandte Physik, Christian-Albrechts-Universität zu Kiel, Kiel, Germany*
[3]*Ruprecht Haensel Laboratory, Kiel University and DESY, Kiel, Germany*
[4]*Experimentelle Physik IV and Würzburg-Dresden Cluster of Excellence ct.qmat, Universität Würzburg, D-97074 Würzburg, Germany*
[5]*National High Magnetic Field Laboratory, Tallahassee, Florida 32310, USA*
[6]*Nuclear Nonproliferation Division, Oak Ridge National Laboratory, Oak Ridge, Tennessee 37831, USA*
[7]*Department of Chemical and Biomedical Engineering, FAMU-FSU College of Engineering, Tallahassee, Florida 32310, USA*

The electronic structure of Weyl semimetals features Berry flux monopoles in the bulk and Fermi arcs at the surface. While angle-resolved photoelectron spectroscopy (ARPES) is successfully used to map the bulk and surface bands, it remains a challenge to explicitly resolve and pinpoint these topological features. Here we combine state-of-the-art photoemission theory and experiments over a wide range of excitation energies for the Weyl semimetals TaAs and TaP. Our results show that simple surface-band-counting schemes, proposed previously to identify nonzero Chern numbers, are ambiguous due to pronounced momentum-dependent spectral weight variations and the pronounced surface-bulk hybridization. Instead, our findings indicate that dichroic ARPES provides an improved approach to identify Fermi arcs but requires an accurate description of the photoelectron final state.

Angle-resolved photoemission spectroscopy (ARPES) [1,2] provides information about the initial state electronic wave functions in the momentum space of crystalline solids [3,4]. The Bloch wave functions enter the measured intensity distributions as the initial state of the photoemission matrix element. The photoemission intensity distribution, which is proportional to the square of the absolute value of this matrix element, in principle, contains crucial information about the topological properties that are in general closely related to momentum dependence of the wave function $\Psi(k)$. At the same time, however, the photoemission matrix element depends on the final state of the emitted photoelectron which complicates the extraction of information about the initial state. The effect of the transition dipole matrix element is often viewed as detrimental as it breaks the quasi-one-to-one correspondence between the measured spectra and occupied band structure. It strongly modulates the momentum- and energy-resolved spectral weight of individual electronic bands and in some cases, can lead up to a complete suppression of photocurrent in certain parts in the momentum space [4,5]. The possibility of complete suppression of the photoemission intensity shows that, in some cases, matrix element effects are absolutely crucial for the interpretation of ARPES spectra.

Topological Weyl semimetals (TWSs) that exhibit massless relativistic fermionic quasiparticles have remained a pivotal topic in condensed matter physics in recent years [6,7]. They contain Weyl points (WPs), i.e., topologically protected crossings of the spin-polarized bulk valence and conduction bands, which appear in pairs of opposite chirality, and are connected by topological surface states referred to as Fermi arcs. The topology in Weyl semimetals (WSMs) manifests itself in the monopole charge of the Berry curvature, i.e., the integral of the latter around a WP is integer quantized reflecting a Chern number of ± 1. Substantial progress in identifying Berry flux monopoles has been made, e.g., using transport experiments [8] or circular dichroism (CD) [9–13] that indicate characteristic spectral weight behavior in surface and bulk states near WPs. However, the ARPES related signatures rely on simplifying assumptions such as two-band systems or a free-electron (FE) like final state in CD [10]. Another approach is to use the chiral edge mode counting criterion relying on the bulk-boundary correspondence, which states that the number of surface Fermi arcs connecting to the WP reflects the net Chern number of the latter projected on the surface Brillouin zone [14]. Based on this, surface-sensitive ARPES measurements have been used to address the projected Chern numbers in the paradigmatic WSM TaAs and TaP [15–17]. However, as we will demonstrate later, strong spectral weight variations in dependence of photon energy and polarization lead to substantial complications and call into question the analysis introduced in Ref. [15].

In this joint experimental and theoretical work, we address the spectral weight variations of surface and bulk states near Weyl nodes and conclude that matrix elements and a proper final state description are important to achieve detailed information about the Bloch states. Our Letter questions previous ARPES-based identification of Fermi arcs and the nonzero Chern number in TaAs that neglected these effects [15]. In the approach presented here, we aimed to combine the chiral-edge mode counting criterion, topological signatures in linear and circular dichroic ARPES measurements, and state-of-the-art photoemission theory in a coherent way and found a more general approach for identifying the Berry flux monopoles combining the *ab initio* depth-sensitive photoemission calculations with experiments in the vacuum ultraviolet (VUV) and soft x-ray (SX) regimes.

The one-step model of photoemission calculations as implemented in the SPR-KKR band structure software package [18], based on Green's function and multiple scattering spin-density matrix formalism, properly includes all the matrix element effect related phenomena. This fully relativistic method gives access to a photoemission signal with an accurate angular variation of ARPES spectral weight caused by an experimental geometry, photon energy, and polarization state or surface termination [19–22]. In addition, an imaginary potential term V_{0i} is added to the single-particle cell potential to simulate lifetime effects in the initial state. The surface sensitivity is addressed by the finite imaginary part V_{0f} of the effective potential for the final state that adequately accounts for the corresponding inelastic mean free path (IMFP). Surface potential is realistically described by a spin-dependent Rundgren-Malmström barrier $V^{\uparrow\downarrow}(z)$ [23]. Within the package it is possible to artificially manipulate the bulk sensitivity of the experiment or to distinguish between the time-reversed low energy electron diffraction (TR-LEED) final state [24,25] and a FE final state that is often used as simplifying assumption in the SX regime (and often necessary for a close relation of CD and Berry curvature). The calculated one-step model spectra use TR-LEED final states unless a FE final state is mentioned specifically. As a basis for the self-consistent field of the bulk TaP and TaAs [Fig. 1(a)] (space group [109]), we have used a lattice constant of 3.318 Å for TaP and 3.435 Å for TaAs. The on-site Coulomb repulsion term can have a significant effect on how well the topological nature of the material is captured by the theoretical model [26]. After performing a set of LDA + U calculations, we conclude that we did not see significant changes in the observables of the photoemission even for Hubbard $U = 5$ eV. This makes us certain that the topology-related conclusions made in this Letter are indeed well captured by our theoretical model [27].

The ARPES experiments in the VUV regime on the TaP single crystals are performed at the MAESTRO end station at beamline 7 of the Advanced Light Source (ALS) using
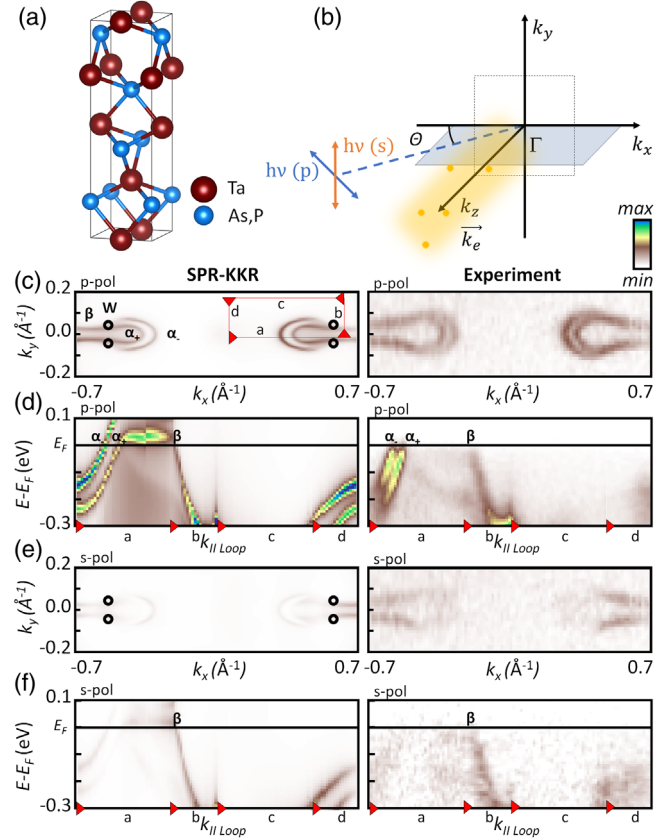

FIG. 1. (a) Crystal structure of TaP and TaAs. (b) Geometrical configuration used both in experiment and SPR-KKR calculations. *p*- or *s*-polarized VUV ($h\nu = 105$ eV) photons are focused onto a freshly cleaved bulk crystal at an angle of incidence of $\Theta = 17°$ (33.25° for the VUV data in Fig. 3). The figures (c) and (e) show constant energy contours (CECs) at E_F taken with *p*- and *s*-polarized VUV light, respectively. For both CECs in (c) and (e), corresponding band structure cuts (d) and (f) were extracted in the anticlockwise direction starting along the k_x direction as represented by the *a-b-c-d* sequence in (c). One-step model photoemission intensity calculations on TaP are on the left and experimental data are on the right.

a photon energy of $h\nu = 105$ eV with linear horizontal and vertical polarization. The plane of incidence of the incoming photons is located in the *xz* plane [Fig. 1(b)] with light coming under an angle $\Theta = 35.25°$. The slit of the Scienta R4000 analyzer is oriented in the same plane as the incoming light. The energy and angular resolution is better than 30 meV and 0.01 $Å^{-1}$ [13]. The SX-ARPES experiments were carried out at ASHPERE III at the Beamline P04 of PETRA III at DESY with circularly polarized light and $h\nu = 590$ eV. The experimental geometry is the same as at the MAESTRO-endstation except for the angle of incidence $\Theta = 17°$. The energy and angle resolution is better than 90 meV and 0.1°. For both experiments the UHV conditions were better than 3×10^{-10} mbar and the sample temperature was lower than 50 K. Let us first consider the band counting argument used in previous

ARPES studies [15–17]. For photon energies in the VUV regime, ARPES is mostly sensitive to the surface states in Ta(As, P) [13,17,28]. Besides the striking agreement in terms of spectral weight of experimental and calculated data, our VUV TaP data in Figs. 1(c)–1(f) demonstrate the importance of matrix-element effects. Figure 1(d) shows a band structure cut along a $k_\parallel$ loop as indicated in Fig. 1(c) for ARPES data taken with p-polarized light. The experimental data are in good agreement with photoemission calculation, and there are three Fermi-level crossings labeled as α_+, α_-, and β. The projected WP enclosed by the curve has a net chirality of $C = +2$ [16]. Thus, based on the bulk-boundary correspondence, the latter should be reflected by the difference of left- and right-moving edge modes $C = N_R - N_L$ [15–17]. However, in our dataset shown in Fig. 1(c) and the corresponding band structure cut in Fig. 1(d), one finds $C = 2 - 1 = +1$, contradicting the theoretical expectation. Even more divergent results are found when considering ARPES data taken with s-polarized light [Figs. 1(e) and 1(f)]. Again, in good agreement between the spin-polarized relativistic Korringa-Kohn-Rostoker calculations and the experimental data, one finds $C = 0$–$1 = -1$, since the photoemission intensity of the surface states "α_+" and "α_-" is almost completely suppressed under these experimental conditions. Two important conclusions can be drawn from these observations: First, there are three surface state features at E_F that connect to the projected WP. The question how this can be reconciled with the bulk Chern number has been discussed previously but remains unclear. Second, the consideration of the mere ARPES intensity alone is not a rigorous proof of the topological invariant. On the one hand, it is not directly evident, which surface states have to be considered in the counting criterion and which do not, i.e., which are topological or trivial surface states, respectively. On the other hand, photoemission matrix element effects can lead to complete intensity suppression of specific features, so that the counting criterion based on a single dataset is not a meaningful approach. In particular, in the dataset of Ref. [15] the feature β is completely suppressed in intensity, leading to $C = 2$ and, thus, to an ostensible agreement with the bulk Chern number.

The issues mentioned above show that considering only the band dispersion is not sufficient to assess the topology in WSMs. Instead, the essential changes of the wave function character as a function of momentum have to be considered [13,29]. It has been shown that the spoon features $\alpha_\pm$ in TaP(001) at $k_y = 0$ are built from P p_x and p_z as well as Ta d_{xz}, $d_{x^2-y^2}$, and d_{z^2} character. In agreement with the enhanced (suppressed) photoemission intensity using p-(s-) polarized light (see Fig. 1), all of these states are even with respect to $y \rightarrow -y$. On the other hand, the neck features β have predominantly odd d_{yz} and d_{xy} character (again in agreement to the polarization-dependent ARPES data in Fig. 1). The characteristic change of orbital character is likely accompanied by a variation of the spin- and orbital-angular momentum which are aligned by spin-orbit coupling (SOC). Because of inversion symmetry breaking (ISB) in the Ta(As, P) bulk crystal structure and at the surface, a sizable orbital angular momentum (OAM) $\langle L \rangle = m_l$ can be formed in the wave functions of both the surface state (SS) and bulk state (BS) [13]. While the even orbitals building up the spoon features can form finite OAM expectation values $m_{y,1} = \pm 1$ ($p_x \pm i p_z$) and $m_{y,2} = \pm 2$ ($2d_{xz} \pm i\sqrt{3}d_{z^2} \pm d_{x^2-y^2}$), the odd d_{yz} and d_{xy} character of β allows for the formation of an additional strong x component of the OAM; $m_{x,2} = \pm 1$ ($d_{yz} \pm i\ d_{xy}$). This picture overall agrees well with the calculated spin texture of the features in [9] and Fig. SM1, and suggests a SOC-induced alignment of OAM and spin. As such, the orbital symmetry change around the projected WP, which in turn leads to the strong spectral modulation in the polarization-dependent ARPES data, is likely accompanied by a change of the OAM (and spin [29]) texture.

The OAM can be addressed more directly using ARPES combined with linear [30] or circular dichroism [9,31]. The former occurs in measurements taken with p-polarized light due to the broken experimental mirror symmetry along $k_x \rightarrow -k_x$, allowing for an asymmetric intensity distribution, which results in the linear dichroism (LD) $\Delta I_{LD} = I(k_x, k_y) - I(-k_x, k_y)$. Within the experimental geometry used [Fig. 1(b)] one finds that the LD is sensitive to the y component of the OAM [30]. Figures 2(a) and 2(b) show the LD results in a Fermi map as measured experimentally and calculated within the SPR-KKR one-step model of photoemission, respectively. Clearly, a LD sign change is observed close to the momenta of the projected WP [13], which is further supported in great detail by the calculated LD pattern [Fig. 2(b)]. This can also be seen in the band structure cut [Figs. 2(e) and 2(f)] through the projected WP along k_x [as labeled by the dashed line in Figs. 2(a) and 2(b)]. The spoon features $\alpha_\pm$ have an opposite sign compared to β suggesting a sign switch of the OAM m_y.

It has been suggested that the strong modulations of the wave functions close to the projected WP arise from a transition of the surface states into surface resonances, i.e., bulklike states with an enhanced probability density at the surface [13]. We will now first explore this transition in more detail by examining the so-called determinant criterion [32,33] and subsequently come back to what this might entail with a change of the LD sign.

Within the one-step model multiple scattering theory a surface barrier which connects the inner potential of the bulk crystal with the vacuum is introduced. Solving the multiple scattering problem of a wavefield between the surface of the semi-infinite bulk crystal and the surface barrier potential requires use of the reflection matrices of the bulk crystal $\mathbf{R}_b$ and the barrier potential $\mathbf{R}_v$. The SS, surface-bulk resonances (SBRs) or BS character can consequently be determined by the determinant criterion using
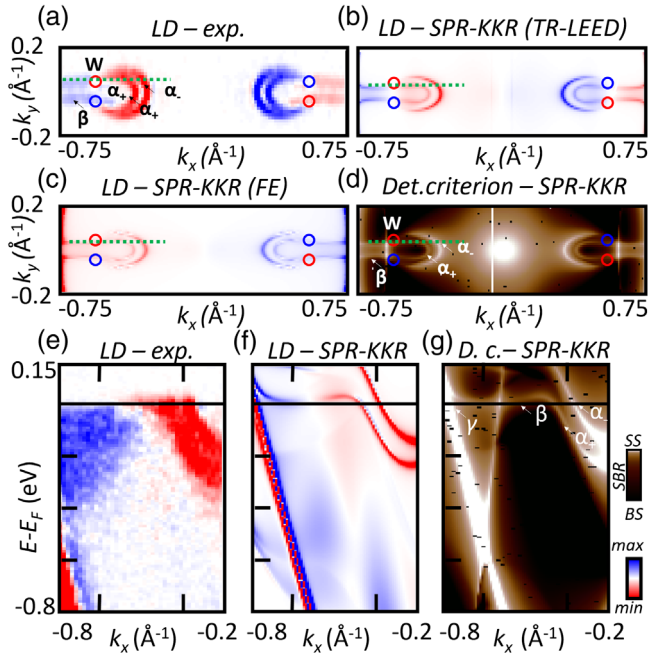
FIG. 2. LD, CD, and determinant criterion in VUV regime on TaP. (a) Experimentally measured LD using the same experimental geometry as described in Fig. 1(b). Calculated LD with the TR-LEED final state (b) and FE final state in (c). The determinant criterion plot for the corresponding CECs is provided by the one-step model (KKR) method in (d). (e) and (f) represent the corresponding $E(k_x)$ cuts marked by the dashed green line in (a) and (b). (g) The $E(k_x)$ plot of the corresponding determinant criterion. The spoon- and neck-shaped features are labeled α_+, α_-, and β correspondingly. The circles denote projected WP. Red and blue colors of WPs indicate opposite chirality.

the value of $|\det(\mathbb{1} - \mathbf{R}_b\mathbf{R}_v)|$ [33]. In the determinant color scale, the smallest values (in white) correspond to the SS being mostly localized between the topmost atomic layer and surface potential. The black states correspond to the BS whereas the SBR states, being partially reflected

from the bulk states are shown in brown color. This *ab initio* tool demonstrates that both the inner and the outer part of the spoon-shaped feature $\alpha_\pm$ in Figs. 2(d) and 2(f) have a clear surface character while the neck feature β is mostly of SBR nature. On the other hand, at the position of the projected WPs, the character of associated photocurrent is clearly bulklike as expected and shows a clear separation of the spoon and neck features. Taken together, the determinant criterion directly shows that $\alpha_\pm$ are real surface states but α_+ smoothly develops from a SS to a SBR β when approaching the projected bulk bands, i.e., more precisely the projected WP.

We now come back to the LD sign change observed at the projected WP, or more generally, to the overall expected change of the OAM texture around these momenta. It has been shown recently, that the OAM of the bulk bands, i.e., the bands forming the Weyl cones, is strongly modulated around the WP [9]. More precisely, complete OAM sign changes occur (see further discussion below) [9]. The LD observed in the surface states hints to an OAM polarization of these as well. In connection with the SS-SBR transition, the modulation of the OAM texture around the projected WP can likely be attributed to an alignment of the surface state OAM with those of the bulks bands when the former develops into SBR.

Similar observation relations between the OAM and CD can be drawn in the SX regime. In Fig. 3(a) we show a sum of photoemission intensities of I_R and I_L with corresponding CD in Fig. 3(b). The crossing of the bands denoted as bs_1 and bs_2 forming a Weyl cone give rise to a WP at their intersection. The measured and calculated CD in Figs. 3(b) and 3(d), respectively, show a distinct sign flip exactly at the crossing of bs_1 and bs_2, which agrees with the sign reversal of the L_x component of OAM [9]. It should be noted that one still sees a dichroic signal coming from the surface states α_+ and α_- in the calculated spectra in Fig. 3(c) and 3(d) which are missing in experiment due
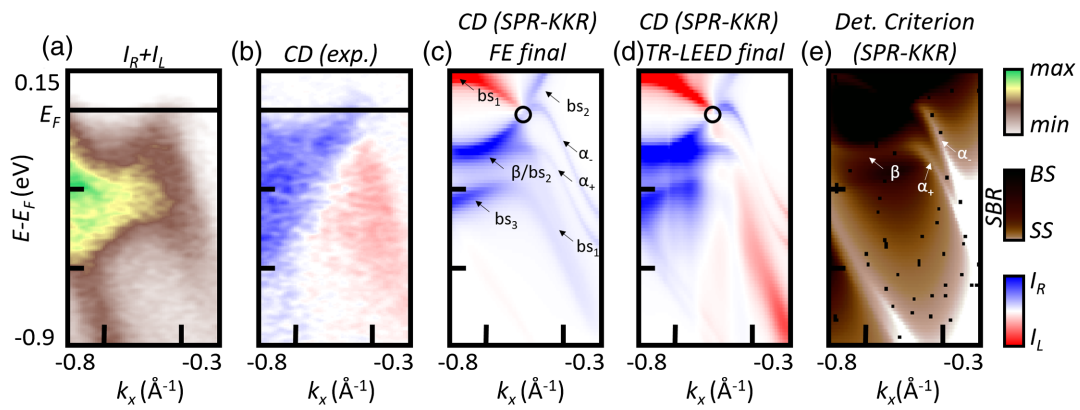

FIG. 3. (a) The sum of intensities measured by left- and right-polarized light in the SX regime at 590 eV in TaAs, (b) The dichroism based on these intensities. (c) The one-step model based calculated dichroism with TR-LEED final state and (d) the calculated CD with FE final state. The cuts were extracted at the k_y position of the WP similarly to the cuts in Figs. 2(e)–2(g). (e) Determinant criterion. The expected position of the WP is marked with a circle; SS, SBR, and BS are marked by arrows.

to high resolution and well resolved corresponding bands in the calculation. The determinant criterion plot in Fig. 3(e) confirms a bulk character of bands denoted as bs_1, bs_2 (partially overlapping with β feature), and bs_3. The bulk character of the corresponding bands is further confirmed by artificial manipulation of the imaginary part V_{0f} of the final state in the Supplemental Material (Fig. SM2) that shows much higher photoemission intensity of the bulk state with lower value of V_{0f} (and therefore higher bulk sensitivity) while the intensity variation of surface states SS_1 and SS_2 changes only slightly.

Based on theoretical predictions of previous works, the relationship between dichroism and OAM is based on FE final state approximation [10,31,34]. In general, dichroic signals are final-state dependent and, thus, the relation between the above mentioned observables and dichroism requires a proper final state description. So far our experimental and theoretical results establish characteristic modulations in the dichroism near the Weyl nodes, both under surface and bulk sensitive conditions. Motivated by the general importance of dichroic ARPES, we will now explore the role of the photoelectron final state for a proper understanding of these modulations. Therefore, we have performed a one-step model calculation using a rigorous TR-LEED as well as a FE final state for both the VUV and SX-ARPES data [compare Figs. 2(b), 2(c) and 3(c), 3(d), respectively]. It is apparent that the LD spectra in Figs. 2(b) and 2(c) do not even qualitatively match. The nonexistent sign flip of LD with the FE final state at the WP does not agree with the experimental dichroism data. As discussed in more detail before, there is again a good agreement between the measured CD [Fig. 3(b)] and the photoemission calculation [Fig. 3(d)] if a TR-LEED state is used in the SX-ARPES case. This texture, in turn, agrees well with the calculated initial state OAM, as shown in [9]. However, using a FE final state, this is not the case: In particular, the experimentally observed CD (OAM) sign change within the lower part of the Weyl cone is not found. Yet, this signature is crucial for nontrivial winding of OAM and Berry curvature around the WP. Taken together, in both cases studied, i.e., the LD on the surface states and the CD on the bulk states, the FE final state approximation does not reproduce the experimental data. Consequently, we conclude that a more realistic description of the final state is needed to explain dichroism by modeling the photoemission matrix element. It immediately follows that the relation between dichroic ARPES and OAM in the initial state, which indeed seems to be quite reliable, cannot be explained within this final state picture.

To conclude, both surface and bulk sensitive ARPES measurements on TaP and TaAs show pronounced spectral weight variations near the Weyl points. As we showed, their presence questions previous ARPES-based identification of nonzero Chern numbers from surface band counting [15]. Our calculations show that understanding these spectral weight variations requires an accurate description of the photoemission matrix element, beyond simplifying assumptions such as the free-electron final state approximation. The importance of the final state description calls for more accurate approximations in real systems beyond a two-band system and FE description [10] to directly relate CD and Berry curvature. In close comparison to theory, ARPES signatures, such as dichroism, yield detailed information about the character of the initial Bloch states near the Weyl points, e.g., with regard to surface or bulk localization and orbital symmetry. These findings will be also relevant to other material classes, such as $MoTe_2$ and WTe_2 where the Weyl character of the band structure remains controversial [12,20,35–37]. More generally, our results push forward the general understanding of dichroic ARPES and its relation to orbital angular momentum and Berry curvature. We believe that after pinpointing the drawbacks and incompleteness of the chiral edge counting criterion, the new methodology presented here not only establishes a new systematic and complete approach for the spectroscopic analysis of the electronic structure in these specific Weyl semimetals, but will find its use also when addressing many other topological quantum materials.

---

[*]jakub.schusser@physik.uni-wuerzburg.de

[1] F. Reinert and S. Hüfner, Photoemission spectroscopy— From early days to recent applications, New J. Phys. **7**, 97 (2005).

[2] S. Hüfner, R. Claessen, F. Reinert, T. Straub, V. N. Strocov, and P. Steiner, Photoemission spectroscopy in metals: Band structure-fermi surface-spectral function, J. Electron Spectrosc. Relat. Phenom. **100**, 191 (1999).

[3] A. Damascelli, Probing the electronic structure of complex systems by ARPES, Phys. Scr. **T109**, 61 (2004).

[4] S. Moser, An experimentalist's guide to the matrix element in angle resolved photoemission, J. Electron Spectrosc. Relat. Phenom. **214**, 29 (2017).

[5] R. P. Day, B. Zwartsenberg, I. S. Elfimov, and A. Damascelli, Computational framework chinook for angle-resolved photoemission spectroscopy, npj Quantum Mater. **4**, 54 (2019).

[6] N. P. Armitage, E. J. Mele, and A. Vishwanath, Weyl and Dirac semimetals in three-dimensional solids, Rev. Mod. Phys. **90**, 015001 (2018).

[7] B. Q. Lv, T. Qian, and H. Ding, Experimental perspective on three-dimensional topological semimetals, Rev. Mod. Phys. **93**, 025002 (2021).

[8] D. M. Mahler, J. B. Mayer, P. Leubner, L. Lunczer, D. Di Sante, G. Sangiovanni, R. Thomale, E. M. Hankiewicz, H. Buhmann, C. Gould, and L. W. Molenkamp, Interplay of Dirac Nodes and Volkov-Pankratov Surface States in Compressively Strained HgTe, Phys. Rev. X **9**, 031034 (2019).

[9] M. Ünzelmann, H. Bentmann, T. Figgemeier, P. Eck, J. N. Neu, B. Geldiyev, F. Diekmann, S. Rohlf, J. Buck, M. Hoesch, M. Kalläne, K. Rossnagel, R. Thomale, T. Siegrist, G. Sangiovanni, D. D. Sante, and F. Reinert, Momentum-space signatures of Berry flux monopoles in the Weyl semimetal TaAs, Nat. Commun. **12**, 3650 (2021).

[10] M. Schüler, U. De Giovannini, H. Hübener, A. Rubio, M. A. Sentef, and P. Werner, Local Berry curvature signatures in dichroic angle-resolved photoelectron spectroscopy from two-dimensional materials, Sci. Adv. **6**, eaay2730 (2020).

[11] S. Cho, J.-H. Park, S. Huh, J. Hong, W. Kyung, B.-G. Park, J. D. Denlinger, J. H. Shim, C. Kim, and S. R. Park, Studying local Berry curvature in 2H-WSe2 by circular dichroism photoemission utilizing crystal mirror plane, Sci. Rep. **11**, 1684 (2021).

[12] K. Hagiwara, P. Rüßmann, X. L. Tan, Y.-J. Chen, K. Ueno, V. Feyer, G. Zamborlini, M. Jugovac, S. Suga, S. Blügel, C. M. Schneider, and C. Tusche, Link between Weyl-fermion chirality and spin texture, arXiv:2205.15252.

[13] C.-H. Min, H. Bentmann, J. N. Neu, P. Eck, S. Moser, T. Figgemeier, M. Ünzelmann, K. Kissner, P. Lutz, R. J. Koch, C. Jozwiak, A. Bostwick, E. Rotenberg, R. Thomale, G. Sangiovanni, T. Siegrist, D. Di Sante, and F. Reinert, Orbital Fingerprint of Topological Fermi Arcs in the Weyl Semimetal TaP, Phys. Rev. Lett. **122**, 116402 (2019).

[14] X. Wan, A. M. Turner, A. Vishwanath, and S. Y. Savrasov, Topological semimetal and Fermi-arc surface states in the electronic structure of pyrochlore iridates, Phys. Rev. B **83**, 205101 (2011).

[15] I. Belopolski *et al.*, Criteria for Directly Detecting Topological Fermi Arcs in Weyl Semimetals, Phys. Rev. Lett. **116**, 066802 (2016).

[16] S.-Y. Xu *et al.*, Experimental discovery of a topological Weyl semimetal state in TaP, Sci. Adv. **1**, e1501092 (2015).

[17] Z. K. Liu, L. X. Yang, Y. Sun, T. Zhang, H. Peng, H. F. Yang, C. Chen, Y. Zhang, Y. F. Guo, D. Prabhakaran, M. Schmidt, Z. Hussain, S. K. Mo, C. Felser, B. Yan, and Y. L. Chen, Evolution of the Fermi surface of Weyl semimetals in the transition metal pnictide family, Nat. Mater. **15**, 27 (2016).

[18] H. Ebert, D. Ködderitzsch, and J. Minár, Calculating condensed matter properties using the KKR-Green's function method—recent developments and applications, Rep. Prog. Phys. **74**, 096501 (2011).

[19] S. Beaulieu, J. Schusser, S. Dong, M. Schüler, T. Pincelli, M. Dendzik, J. Maklar, A. Neef, H. Ebert, K. Hricovini, M. Wolf, J. Braun, L. Rettig, J. Minár, and R. Ernstorfer, Revealing Hidden Orbital Pseudospin Texture with Time-Reversal Dichroism in Photoelectron Angular Distributions, Phys. Rev. Lett. **125**, 216404 (2020).

[20] M. Fanciulli, J. Schusser, Min.-I. Lee, Z. E. Youbi, O. Heckmann, M. C. Richter, C. Cacho, C. Spezzani, D. Bresteau, J.-F. Hergott, P. D'Oliveira, O. Tcherbakoff, T. Ruchon, J. Minár, and K. Hricovini, Spin, time, and angle resolved photoemission spectroscopy on WTe2, Phys. Rev. Res. **2**, 013261 (2020).

[21] R. Ono, A. Marmodoro, J. Schusser, Y. Nakata, E. F. Schwier, J. Braun, H. Ebert, J. Minár, K. Sakamoto, and P. Krüger, Surface band characters of the Weyl semimetal candidate material MoTe2 revealed by one-step angle-resolved photoemission theory, Phys. Rev. B **103**, 125139 (2021).

[22] S. Beaulieu, M. Schüler, J. Schusser, S. Dong, T. Pincelli, J. Maklar, A. Neef, F. Reinert, M. Wolf, L. Rettig, J. Minár, and R. Ernstorfer, Unveiling the orbital texture of 1T-TiTe2 using intrinsic linear dichroism in multidimensional photoemission spectroscopy, npj Quantum Mater. **6**, 93 (2021).

[23] J. Rundgren and G. Malmstrom, Transmission and reflection of low-energy electrons at the surface barrier of a metal, J. Phys. C **10**, 4671 (1977).

[24] J. Braun, J. Minár, H. Ebert, M. I. Katsnelson, and A. I. Lichtenstein, Spectral Function of Ferromagnetic 3 d Metals: A Self-Consistent LSDA + DMFT Approach Combined with the One-Step Model of Photoemission, Phys. Rev. Lett. **97**, 227601 (2006).

[25] C. N. Berglund and W. E. Spicer, Photoemission studies of copper and silver: Theory, Phys. Rev. **136**, A1030 (1964).

[26] N. Aryal and E. Manousakis, Importance of electron correlations in understanding photoelectron spectroscopy and Weyl character of $MoTe_2$, Phys. Rev. B **99**, 035123 (2019).

[27] See Supplemental Material at http://link.aps.org/supplemental/10.1103/PhysRevLett.129.246404 for more detailed information about the theoretical calculations.

[28] B. Q. Lv, H. M. Weng, B. B. Fu, X. P. Wang, H. Miao, J. Ma, P. Richard, X. C. Huang, L. X. Zhao, G. F. Chen, Z. Fang, X. Dai, T. Qian, and H. Ding, Experimental Discovery of Weyl Semimetal TaAs, Phys. Rev. X **5**, 031013 (2015).

[29] Y. Sun, S.-C. Wu, and B. Yan, Topological surface states and Fermi arcs of the noncentrosymmetric Weyl semimetals TaAs, TaP, NbAs, and NbP, Phys. Rev. B **92**, 115428 (2015).

[30] M. Ünzelmann, H. Bentmann, P. Eck, T. Kißlinger, B. Geldiyev, J. Rieger, S. Moser, R. C. Vidal, K. Kißner, L. Hammer, M. A. Schneider, T. Fauster, G. Sangiovanni, D. Di Sante, and F. Reinert, Orbital-Driven Rashba Effect in a Binary Honeycomb Monolayer AgTe, Phys. Rev. Lett. **124**, 176401 (2020).

[31] J. H. Park, C. H. Kim, J. W. Rhim, and J. H. Han, Orbital Rashba effect and its detection by circular dichroism angle-resolved photoemission spectroscopy, Phys. Rev. B **85**, 195401 (2012).

[32] C. Seibel, H. Bentmann, J. Braun, J. Minár, H. Maaß, K. Sakamoto, M. Arita, K. Shimada, H. Ebert, and F. Reinert, Connection of a Topological Surface State with the Bulk Continuum in Sb2Te3(0001), Phys. Rev. Lett. **114**, 066802 (2015).

[33] J. Braun and M. Donath, Contest between surface resonances and surface states at 3d ferromagnets, Europhys. Lett. **59**, 592 (2002).

[34] S. R. Park, J. Han, C. Kim, Y. Y. Koh, C. Kim, H. Lee, H. J. Choi, J. H. Han, K. D. Lee, N. J. Hur, M. Arita, K. Shimada, H. Namatame, and M. Taniguchi, Chiral Orbital-Angular Momentum in the Surface States of Bi2Se3, Phys. Rev. Lett. **108**, 046805 (2012).

[35] J. Jiang, Z. Liu, Y. Sun, H. Yang, C. Rajamathi, Y. Qi, L. Yang, C. Chen, H. Peng, C.-C. Hwang, S. Sun, S.-K. Mo, I. Vobornik, J. Fujii, S. Parkin, C. Felser, B. Yan, and Y. Chen, Signature of type-II Weyl semimetal phase in MoTe2, Nat. Commun. **8**, 13973 (2017).

[36] P. Li, Y. Wen, X. He, Q. Zhang, C. Xia, Z.-M. Yu, S. A. Yang, Z. Zhu, H. N. Alshareef, and X.-X. Zhang, Evidence for topological type-II Weyl semimetal WTe2, Nat. Commun. **8**, 2150 (2017).

[37] S. Lee, J. Jang, S.-I. Kim, S.-G. Jung, J. Kim, S. Cho, S. W. Kim, J. Y. Rhee, K.-S. Park, and T. Park, Origin of extremely large magnetoresistance in the candidate type-II Weyl semimetal MoTe2x, Sci. Rep. **8**, 13937 (2018).

[38] H. Ebert *et al.*, http://ebert.cup.uni-muenchen.de/SPRKKR.